ACS NANO

www.acsnano.org

ARTICLE

Ultra-Wideband Mid-Infrared Chalcogenide Suspended Nanorib Waveguide Gas Sensors with Exceptionally High External Confinement Factor beyond Free-Space

Mingquan Pi, Chuantao Zheng,* Huan Zhao, Zihang Peng, Gangyun Guan, Jialin Ji, Yijun Huang, Yuting Min, Lei Liang, Fang Song, Xue Bai, Yu Zhang,* Yiding Wang, and Frank K. Tittel

Cite This: *ACS Nano* 2023, 17, 17761−17770

Read Online

ACCESS | Metrics & More | Article Recommendations | Supporting Information

ABSTRACT: **On-chip waveguide sensors are potential candidates for deep-space exploration because of their high integration and low power consumption. Since the fundamental absorption of most gas molecules exists in the mid-infrared (e.g., 3−12 μm), it is of great significance to fabricate wideband mid-infrared sensors with high external confinement factor (ECF). To overcome the limited transparency window and strong waveguide dispersion, a chalcogenide suspended nanorib waveguide sensor was proposed for ultra-wideband mid-infrared gas sensing, and three waveguide sensors (WG_1−WG_3) with optimized dimensions exhibit a wide waveband of 3.2−5.6 μm, 5.4−8.2 μm, and 8.1−11.5 μm with exceptionally high ECFs of 107−116%, 107−116%, and 116−128%, respectively. The waveguide sensors were fabricated by a two-step lift-off method without dry etching to reduce the process complexity. Experimental ECFs of 112%, 110%, and 110% were obtained at 3.291 μm, 4.319 μm, and 7.625 μm, respectively, through methane (CH_4) and carbon dioxide (CO_2) measurements. A limit of detection of 5.9 ppm was achieved for an averaging time of 64.2 s through the Allan deviation analysis of CH_4 at 3.291 μm, leading to a comparable noise equivalent absorption sensitivity of 2.3 × 10^{-5} cm^{-1} $Hz^{-1/2}$ as compared to the hollow-core fiber and on-chip gas sensors.**

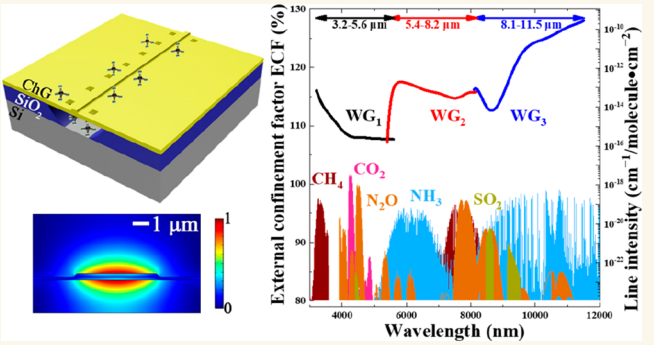

KEYWORDS: *wideband gas sensor, lift-off method, chalcogenide waveguide, suspended waveguide, on-chip gas detection, waveguide sensor*

Most gas molecules show stronger absorption in the mid-infrared (MIR, 2.5−20 μm) than that in the near-infrared (NIR, 0.8−2.5 μm). Both discrete and on-chip waveguide gas sensors based on MIR absorption spectroscopy have high selectivity, good sensitivity, and fast response due to the unique absorption fringe of gaseous analyte.[1−10] Compared to discrete MIR gas measurement, on-chip gas sensing is more suitable for microminiaturized, lightweight, and low power-consumption in situ gas measurement in deep-space (e.g., air in Mars).[11−15] Therefore, the development of an on-chip waveguide gas sensor with wideband and high sensitivity is of great significance for the application of multigas detection in the MIR region.

On one aspect, waveband characteristics of an on-chip waveguide sensor are generally determined by the transparent window of the used waveguide material platform. To date, the reported gas sensor platforms are generally based on silicon (Si) and chalcogenide (ChG) glass. A silicon-on-insulator (SOI) platform with complementary metal oxide semiconductor (CMOS) compatible fabrication process is more suitable for gas measurement below 4 μm because of large absorption loss of silica (SiO_2) in the MIR beyond 4 μm.[16,17] Compared to SOI, the wide transparency window of ChG glass is as large as 1−20 μm with a refractive index of >2.[18−23] Therefore, ChG glass based photonics shows broad application prospects for gas measurement within a wide wavelength

Received: March 24, 2023
Accepted: June 23, 2023
Published: June 28, 2023

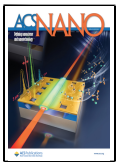

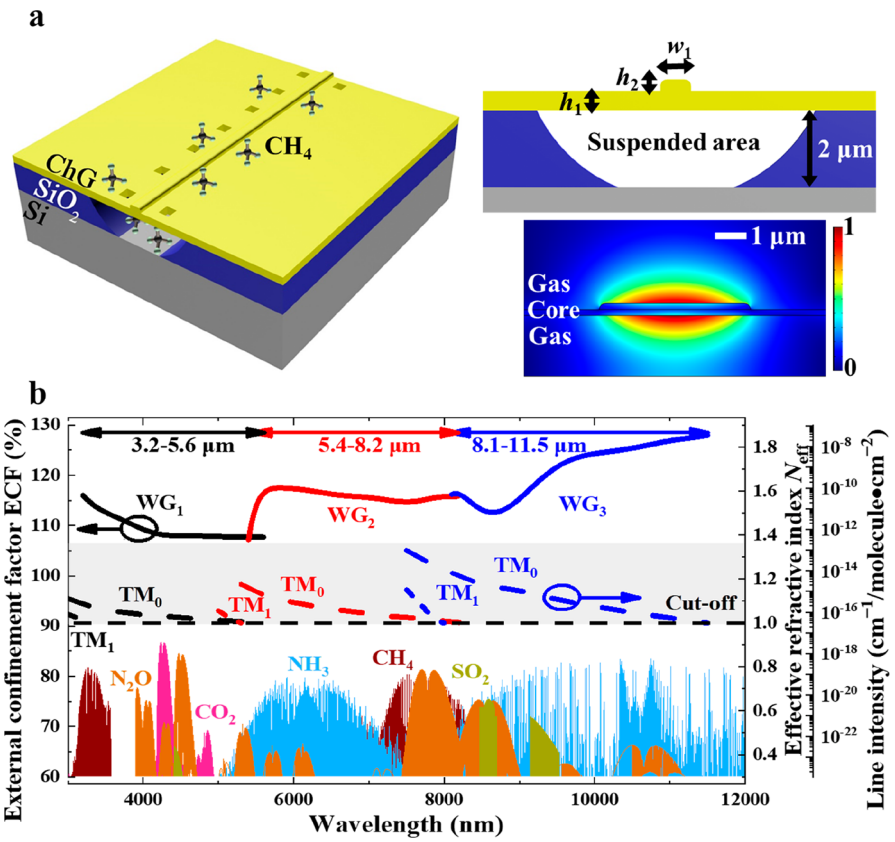

Figure 1. (a) 3D and cross-sectional diagrams of the ChG suspended nanorib waveguide and optical field distribution diagram at 3291 nm. (b) Curves of ECF and N_{eff} of three quasi-TM mode suspended waveguides and line intensity of different gases versus wavelength.

range, which covers the fundamental frequency absorption of most gas molecules.

On another aspect, the external confinement factor (ECF), also named the evanescent field confinement factor, directly affects gas detection sensitivity. For a free-space optical gas sensor, ECF = 1. For a waveguide gas sensor, ECF is generally determined by the mode fraction in the analyte (target gas) for interaction over the waveguide cross-section. Rectangular and rib waveguides with a small ECF (<30%) are the most commonly reported evanescent field sensors.[24] Although a slot waveguide can achieve a large ECF, the increased scattering loss of the side wall leads to the decrease of output power.[25] Different from the above structures, a suspended waveguide makes full use of the bottom area of the core layer for evanescent field sensing, resulting in a larger ECF.[26−28] As proofs of such structure, a previously reported tantalum pentoxide (Ta_2O_5) suspended waveguide sensor at 2.566 μm for acetylene (C_2H_2) detection[26] and an SOI suspended comb waveguide sensor at 7.33 μm for acetone detection[6] obtained high ECFs of 107% and 113%, respectively. So a suspended waveguide with enhanced light−gas interaction is more suitable for on-chip sensing due to the compensation for the influences of unavoidable optical loss and short interaction length. However, the wavelength dependency characteristics of ECF have not been investigated for suspended waveguide sensors in detail, which is important to evaluate the operating waveband of such a structure for practical gas measurement.

Combining the above two aspects, aiming at both wideband and sensitive MIR on-chip gas measurement, a ChG suspended nanorib waveguide sensor structure is proposed with a detailed characterization on both the wavelength dependency of ECF and the wideband gas sensing performance. Three optimized waveguide gas sensors with the same suspended structure but different dimensional parameters exhibit an ultrawide waveband covering 3.2−5.6 μm, 5.4−8.2 μm, and 8.1−11.5 μm, respectively, with exceptionally high ECFs of 107−128% over this wide range. Moreover, until presently, the reported ChG suspended microcavity waveguide sensors[29−31] and the suspended Ta_2O_5[26] and SOI sensors[6] were all fabricated by dry etching. Compared to this technique, the lift-off method shows the merits of reducing cost and fabrication complexity as well as using no dedicated equipment. Thus, a two-step lift-off method without dry etching is presented to fabricate the ChG suspended nanorib waveguide sensor. Detailed methane (CH_4) and carbon dioxide (CO_2) measurements at 3.291, 4.319, and 7.625 μm verify the wideband and sensitive detection ability of the ChG waveguide sensor structure.

RESULTS AND DISCUSSION

Optimization of Waveguide Structure. The single-mode and light-guiding conditions of the waveguide limit the operating waveband of the waveguide sensor. The ECF, effective refractive index N_{eff}, and optical field distribution are obtained by COMSOL Multiphysics. The ECF is determined by the group index n_g and the spatial confinement of the energy density over the cross-section, expressed as[32]

$$\mathrm{ECF} = \frac{n_g \iint_{\mathrm{analyte}} \varepsilon(x,y)|E(x,y)|^2 \mathrm{d}x\mathrm{d}y}{\iint_{\mathrm{total}} \varepsilon(x,y)|E(x,y)|^2 \mathrm{d}x\mathrm{d}y} \quad (1)$$

https://doi.org/10.1021/acsnano.3c02699
ACS Nano 2023, 17, 17761−17770

where E and ε are electric field and permittivity, respectively. n_g is the ratio of the vacuum velocity of light to the group velocity of light in the waveguide, which has the effect of slowing the propagation of the guided mode.[32] Since the output voltage from the detector is proportional to the output power from the waveguide, the gas absorption of the waveguide sensor obeys the Lambert−Beer law, shown as[1,2]

$$V = V_0 \exp(-\mathrm{ECF}\alpha_{\mathrm{CH4}}CL) \quad (2)$$

where α_{CH4} and C are the absorption coefficient of CH_4 and gas concentration, respectively; L is the sensing waveguide length; and V and V_0 are the output voltage from the detector with the target gas absorption and the voltage with no gas absorption, respectively.

As a commonly used nonsuspended waveguide, rectangular waveguide is used as an example to illustrate the problems of such a waveguide. Based on Figure S1, only a small part of light in the gas region can be used for gas sensing and the ECF is <20%, and the single-mode condition is satisfied within a wavelength range of 3.2−4 μm. Compared to a suspended waveguide, the refractive index difference between the core and the lower cladding layer of a nonsuspended waveguide (e.g., rectangular waveguide) is smaller, resulting in a weak optical confinement. Therefore, as the wavelength increases, the mode field is more likely to move to the lower cladding layer with low refractive index, leading to mode cutoff due to the decrease of N_{eff}. For a suspended waveguide, the target gas with a low refractive index has a strong confinement on mode field in the suspended core layer, generating a weak waveguide dispersion. So the strong dispersion of the nonsuspended waveguide limits the wideband sensing application.

To solve the problems of narrow operating waveband and low ECF of nonsuspended waveguides, a ChG suspended nanorib waveguide structure was proposed. The three-dimensional (3D) structure and cross-sectional diagram of the ChG suspended nanorib waveguide are shown in Figure 1a. $Ge_{28}Sb_{12}Se_{60}$ with a refractive index of ∼2.6 at the MIR band was used as the core layer. The transparency range of $Ge_{28}Sb_{12}Se_{60}$ is 1−12 μm. The target gas (e.g., CH_4 and CO_2) with a refractive index of ∼1.0 was used as the upper cladding layer and lower cladding layer. The oxide layer of the Si substrate was 2 μm. The key structural parameters of the suspended nanorib waveguide include the planar layer thickness (h_1), the nanorib height (h_2), and the nanorib width (w_1).

Considering the waveguide dispersion and single-mode propagation, we optimized three ChG suspended waveguides with the same structure but different dimensional parameters to cover the operating wavelength range of 3−12 μm and to obtain high ECF over the whole range. The three waveguides are named WG_1, WG_2, and WG_3, and the optimized process can be seen in Supporting Information S2. Curves of ECF and N_{eff} of the three quasi-TM mode (i.e., the polarization mode of the interband cascade laser (ICL) and quantum cascade laser (QCL)) suspended waveguides and absorption line intensity of different gas species versus wavelength are shown in Figure 1b. Their operating wavebands of the three single-mode waveguide cover 3.2−5.6 μm, 5.4−8.2 μm, and 8.1−11.5 μm, respectively, which cover most gas absorption bands. Also, the operating bandwidth of the ChG suspended nanorib waveguide is >3 times larger than that of the nonsuspended waveguide because of the relatively weak waveguide dispersion. The ECFs of the three waveguides are in the range of 107−116%, 107−116%, and 116−128%, respectively. The structural parameters and wideband characteristics of the three ChG nanorib suspended waveguide are shown in Table 1. The optical field distribution at 3291 nm shown in Figure 1a indicates sufficient areas for light−gas interaction.

Table 1. Structure Parameters and Wideband Characteristics of the Three ChG Nanorib Suspended Waveguides

Waveguide	h_1 (nm)	h_2 (nm)	w_1 (μm)	Operating waveband (μm)	ECF (%)
WG_1	200	200	5	3.2−5.6	107−116, 115 (@3291 nm), 112 (@4319 nm)
WG_2	400	400	5	5.4−8.2	107−116, 115 (@7625 nm)
WG_3	700	700	5	8.1−11.5	116−128

Waveguide Morphology. The ChG waveguide can be fabricated without dry etching, which reduces the need for dedicated etching equipment and effectively reduces cost.[33] We proposed a two-step lift-off method fabrication process of the ChG suspended nanorib waveguide, as shown in Figure 2a. The planar layer with etching holes was fabricated by the first-step lift-off method. Then the ChG nanorib was fabricated by the second-step lift-off method. Finally, the suspended waveguide structure was formed by a 40% HF wet etching. Details of the fabrication process are shown in the Methods. A top-view scanning electron microscopy (SEM, JSM-7500F, JEOL) image of WG_1 is shown in the inset of Figure 2a. As can be seen, the widths of the nanorib and etching hole are 5 and 6 μm, respectively. The SEM images of the cross-sectional structure of the three waveguides are shown in Figure 2b−d. The core sizes of the three waveguides are consistent with the optimization results. The cross-sectional structure shows that sufficient suspended area can be obtained by relying on a single row of etching holes, and two additional etching holes on the other row are used to assist in the alignment of the second lithography process. The suspended nanorib waveguides with different thicknesses show no collapse, indicating the feasibility of the two-step lift-off method for fabricating the suspended structure and the ability for MIR wideband application.

Gas Sensing Results. A simplified structure of the gas sensing system diagram as well as the signal diagrams of the sensing process are shown in Figure 3. Here, the sensing signal can be the absorbance signal under direct absorption spectroscopy (DAS) or the second harmonic ($2f$) signal under wavelength modulation spectroscopy (WMS). Compared with DAS, WMS can suppress system noise (e.g., $1/f$ noise) and increase the signal-to-noise ratio (SNR) using coherent detection.[34] The sensing theory of WMS can be seen in Supporting Information S4. To compare the two sensing schemes at the same time, the rising edge of the triangular-wave driving signal was superimposed with a high-frequency sine-wave modulation signal for WMS measurement and the falling edge of the triangular-wave without modulation was used for DAS measurement.

The CH_4 sensing experiment at 3291 nm was performed by WG_1 to illustrate the advantages of the suspended waveguide and WMS. The absorption spectrum of relatively flat environmental H_2O coincides with the absorption line of CH_4 (Figure S3a). Under the temperature of 298.15 K and the

https://doi.org/10.1021/acsnano.3c02699
ACS Nano 2023, 17, 17761−17770

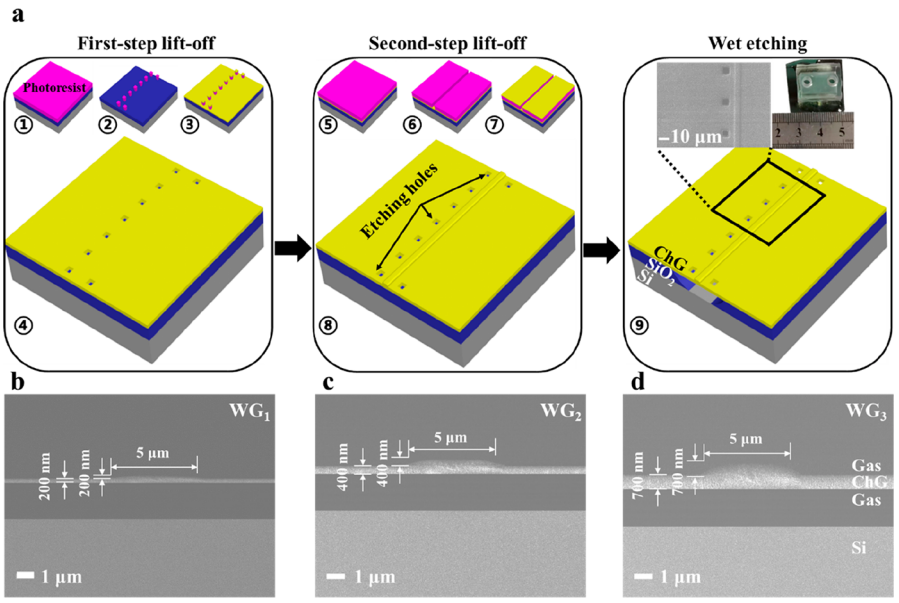

Figure 2. (a) Two-step lift-off method fabrication process of the ChG suspended nanorib waveguide. Inset: Top-view SEM image of WG_1 and the waveguide sensor bonding to a PDMS gas cell. (b–d) SEM images of the cross-sectional structure of (b) WG_1, (c) WG_2, and (d) WG_3.

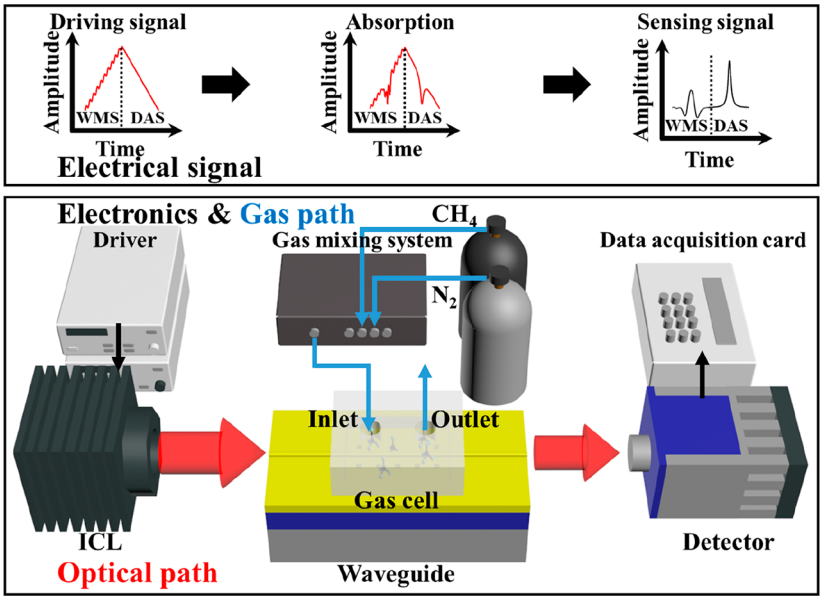

Figure 3. Simplified structure of the gas sensing system diagram and the signal diagrams of the sensing process.

pressure of 10^5 Pa, within the relative humidity range of 0–100%, the H_2O concentration is <4%. The simulated cross interference characteristics of H_2O to CH_4 are shown in Figure S3b, where the target CH_4 concentration is 5 ppm. Because the absorption line of H_2O is relatively flat, H_2O absorption has no effect on DAS results. Because the absorption of H_2O decreases the baseline amplitude, the detected CH_4 concentration based on WMS decreases with the increase of H_2O concentration, which shows an ultrasmall cross interference factor of -8×10^{-10}. Therefore the selected absorption line avoids the influence of H_2O under the two measurement schemes. A more detailed sensing system diagram can be seen in Figure S4. The length of the suspended waveguide for gas sensing is 1 cm. A polydimethylsiloxane (PDMS) gas cell is bonded on the chip for gas injection and ejection, which is shown in the inset of Figure 2a. Details of the gas sensing experimental setup can be seen in the Methods. The propagation loss of WG_1 was determined to be 4.5 dB/cm based on the cutback method in pure nitrogen (N_2) environment.

Another free-space gas cell with an optical path length of 5 cm (Figure S5) was used to experimentally evaluate ECF. ECF can be determined by the ratio between the measured sensing signal using WG_1 and the signal using the free-space gas cell, and the products of the optical path length and gas concentration should be the same under the two measurement cases. The triangular-wave signal frequency was 10 Hz. In order to suppress the $1/f$ noise, the frequency of the sine-wave signal should be as large as possible. However, considering the maximum data sampling rate of the data acquisition card (2 Msps), the sine-wave signal frequency was set to 5 kHz and the data sampling rate was 100 ksps to increase the extraction

https://doi.org/10.1021/acsnano.3c02699
ACS Nano 2023, 17, 17761–17770

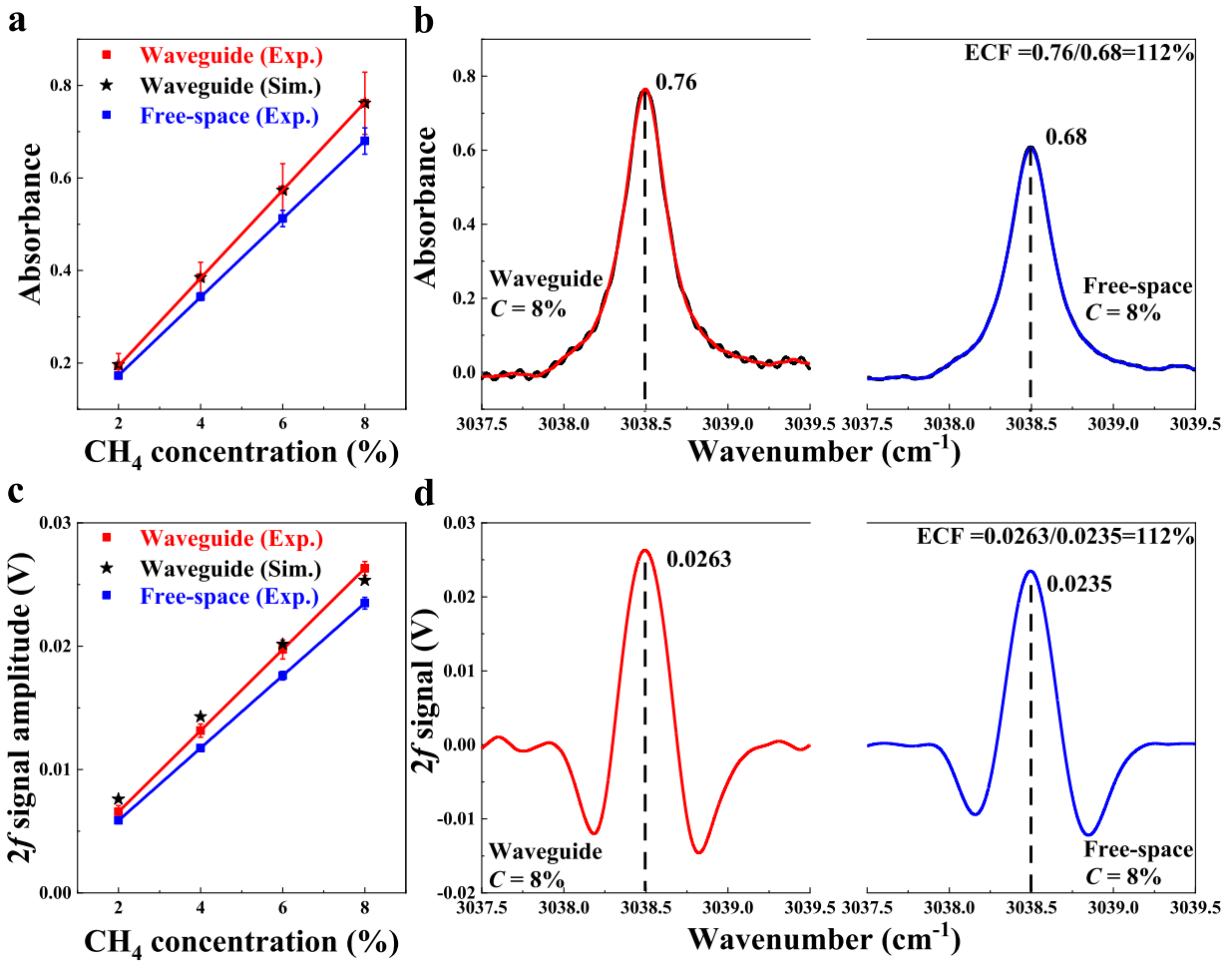

Figure 4. (a) Experimental (red) and simulated (black) data dots of the absorbance of the 1-cm-long waveguide sensor versus CH_4 concentration and the linear fitting curve. Experimental data dots of the absorbance of the 1-cm-long free-space absorption (blue) versus CH_4 concentration and the linear fitting curve. (b) Under an 8% CH_4 concentration level and an optical path length of 1 cm, the measured absorbance signal using the waveguide sensor (red) and the free-space gas sensor (blue). (c) Experimental (red) and simulated (black) data dots of the 2*f* signal amplitude of the 1-cm-long waveguide sensor versus CH_4 concentration and the linear fitting curve. Experimental data dots of the 2*f* signal amplitude from the 1-cm-long free-space absorption (blue) versus CH_4 concentration and the linear fitting curve. (d) Under an 8% CH_4 concentration level and an optical path length of 1 cm, the measured 2*f* signal using the waveguide sensor (red) and the free-space gas sensor (blue).

accuracy of the 2*f* signal (10 kHz). The laser can also be modulated at other suitable frequencies allowed by the data sampling and processing system. The modulation amplitude was optimized for the WMS measurement (Figure S6). The driving current range of the ICL was 40−60 mA, and the optimized modulation amplitude was 0.03 mV.

In DAS measurement, experimental data dots of the absorbance achieved by the 1-cm-long waveguide sensor as well as the normalized absorbance by the 1-cm-long free-space absorption versus CH_4 concentration and their linear fitting curves are shown in Figure 4a. The error bar is related to the accuracy of the gas dilution system. The calibrated relative error of the gas mixing system is ∼5%. Increasing the CH_4 concentration will lead to the increase of the absolute concentration error, and therefore, the size of the error bar becomes larger. At a CH_4 concentration level of 8%, the measured absorbance signal of the waveguide sensor system and the 1-cm-long free-space absorbance signal are shown in Figure 4b. According to the ratio between the obtained absorbances at 3038.5 cm^{-1}, the ECF of WG_1 was determined to be 112%. The difference between the simulation (115%) and experimental results (112%) of ECF probably results from the fabrication error.

In the WMS experiment, the 2*f* signal amplitude was derived by a LabVIEW based lock-in amplifier with an integral time of 22 ms. Since the 2*f* signal amplitude is related to optical power,[5] the output power from the free-space gas cell was adjusted to be consistent with the output power of the waveguide through a linear polarizer. This is required for a reasonable comparison and estimation of ECF. Experimental data dots of the 2*f* signal amplitude of the waveguide sensor and the normalized 2*f* signal amplitude of the 1-cm-long free-space absorption versus CH_4 concentration and their linear fitting curves are shown in Figure 4c. At a CH_4 concentration level of 8%, curves of the measured 2*f* signal using the waveguide sensor and the normalized 2*f* signal of the free-space absorption are shown in Figure 4d. Using the ratio between the 2*f* signal amplitude, an enhancement ECF of 112% was obtained, which is consistent with the result of DAS. In addition, a good agreement can be found between the simulated sensing signal and the experimental result under different concentration levels in Figure 4a and c.

https://doi.org/10.1021/acsnano.3c02699
ACS Nano 2023, 17, 17761−17770

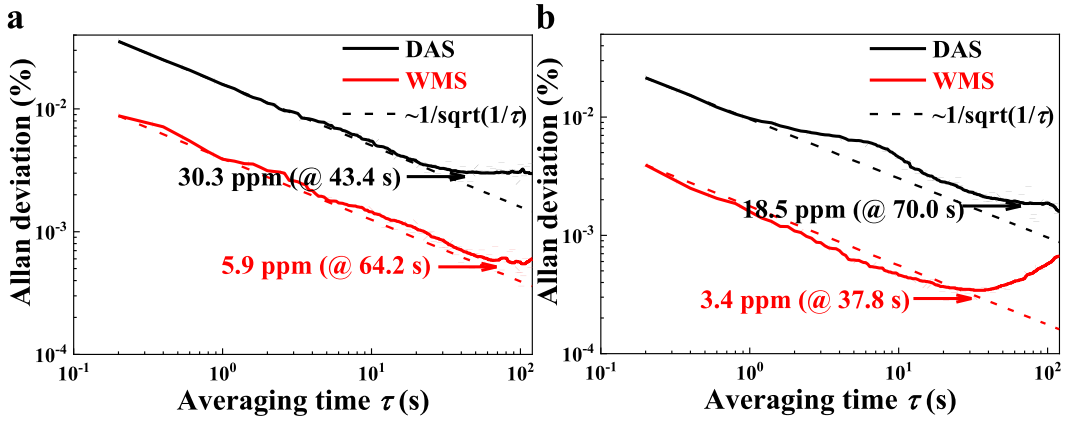

Figure 5. Allan deviation curves obtained by (a) WG_1 and (b) the free-space sensor based on DAS and WMS.

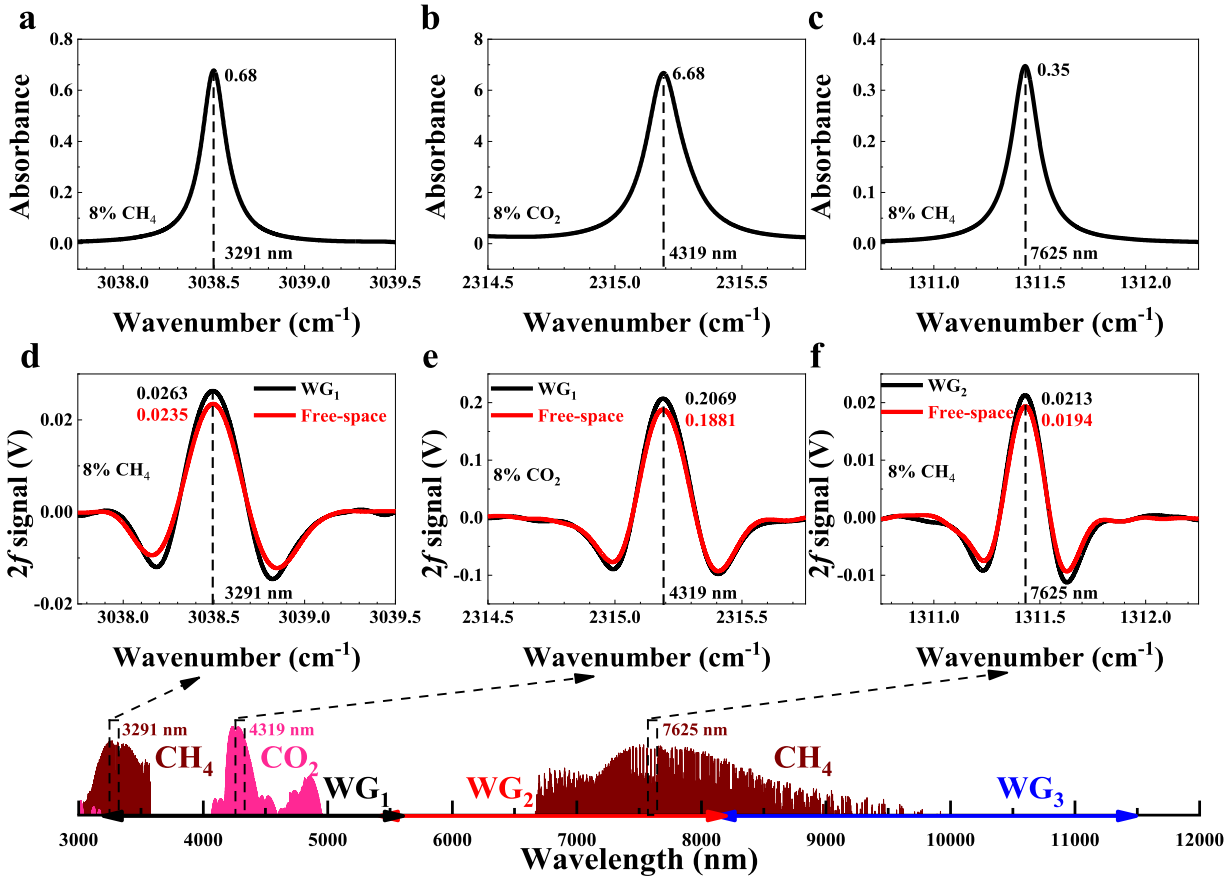

Figure 6. (a–c) Absorbance curves of (a) CH_4 at 3291 nm, (b) CO_2 at 4319 nm, and (c) CH_4 at 7625 nm obtained from the HITRAN database, where the concentration level is 8% and the optical path length is 1 cm. (d–f) Measured 2*f* signal results by the three ChG suspended nanorib waveguides and the free-space optical sensor at (d) 3291, (e) 4319, and (f) 7625 nm.

An Allan deviation analysis was performed in pure N_2 environment for 10 min to evaluate the limit of detection (LoD). The Allan deviation curves obtained by WG_1 are shown in Figure 5a. The LoD values obtained by DAS and WMS are 355.6 and 88.1 ppm at the averaging time (τ) of 0.2 s. The LoD of the DAS measurement is 30.3 ppm with an optimum averaging time of 43.4 s. The LoD of the WMS measurement is 5.9 ppm with an optimum averaging time of 64.2 s, which is ~5 times smaller than that of DAS. The Allan deviation curves obtained by the free-space sensor are shown in Figure 5b. The LoD is 18.5 ppm with an optimum averaging time of 70.0 s for the DAS measurement and 3.4 ppm with an optimum averaging time of 37.8 s for the WMS measurement, respectively. With the same measurement scheme, the LoD of the waveguide sensor is larger than that of the free-space sensor because of the larger noise level of the waveguide mode coupling system. This can be solved by monolithic integration of the laser, sensing waveguide, and detector. For the WMS measurement, the waveguide sensor shows a similar level in noise equivalent absorption sensitivity (NEAS) of 2.3×10^{-5} cm^{-1} $Hz^{-1/2}$ (see Supporting Information S6), as when compared to those of the hollow-core fiber based gas sensor of 2.4×10^{-4} cm^{-1} $Hz^{-1/2}$ and the on-chip SOI gas sensor of 8.7×10^{-5} cm^{-1} $Hz^{-1/2}$.[35]

https://doi.org/10.1021/acsnano.3c02699
ACS Nano 2023, 17, 17761–17770

Wideband Sensing Characteristics. The wideband gas sensing characteristics of the ChG suspended nanorib waveguides are analyzed based on WMS. CO_2 with an absorption at 4319 nm was detected using another distributed feedback ICL with an emission wavelength at 4319 nm, and CH_4 with an absorption at 7625 nm was measured using a distributed feedback QCL with the same wavelength. The simulated absorbance curves of CH_4 at 3291 nm, CO_2 at 4319 nm, and CH_4 at 7625 nm obtained from the HITRAN database[36] are shown in Figure 6a–c, where their concentration levels are 8% and the optical path lengths are 1 cm. Based on WMS, the measured 2*f* signals using WG_1, WG_2, and the free-space optical sensor are shown in Figure 6d–f. The ECF of WG_1 at 4319 nm and the ECF of WG_2 at 7625 nm are both 110%, which is smaller than the theoretical result. The LoD can also be calculated by the SNR, expressed as[5]

$$\mathrm{LoD} = \frac{C}{\mathrm{SNR}} = \frac{C}{\max(2f)/n_{1\sigma}} \tag{3}$$

here $\max(2f)$ is the peak amplitude of the 2*f* signal; and $n_{1\sigma}$ is the 1σ noise $\max(2f)$, which is related to the system noise. The LoD values of CH_4 at 3291 nm, CO_2 at 4319 nm, and CH_4 at 7625 nm are calculated as 103, 140, and 194 ppm. The LoD of CH_4 at 3291 nm based on eq 3 is on the same level as the Allan deviation result (88.1 ppm) at an averaging time of 0.2 s in Figure 5a.

Absorption saturation occurs when the absorbing transition is larger than the relaxation rate.[37] The maximum absorption saturation optical power values of WG_1 at 3291 and 4319 nm and WG_2 at 7625 nm are calculated as 67, 4, and 44 mW for linear optical response. The calculation details can be seen in Supporting Information S7. During gas measurement, strict control of incident power into the waveguide is required.

Low N_{eff} of the suspended waveguide can reduce the Fresnel reflections between the waveguide cross-section and the air to suppress the etalon effect. The reflectivity *R* values between WG_1, WG_2, and the air are 0.001479 (3291 nm), 0.000218 (4319 nm), and 0.000098 (7625 nm), respectively (Supporting Information S8). The N_{eff} of a nonsuspended ChG waveguide in our previous work[3] is as large as 1.82, resulting in a reflectivity of $R = 0.084553$. Therefore, the reflectivity of the suspended waveguide decreases by 57 times compared to that of the nonsuspended ChG waveguide, resulting in an improved ability for suppressing the etalon effect. The above MIR wideband sensing characteristics of the ChG suspended nanorib waveguide sensors are summarized in Table 2.

Comparison and Discussion. A comparison between the ChG suspended nanorib waveguide CH_4 sensor and the experimental results of other MIR waveguide CH_4 sensors is shown in Table 3. All of the ChG waveguides in Table 3 were fabricated by the lift-off method. Though the optical loss of the ChG suspended waveguide is larger than those of other ChG rectangular waveguides in our previous work,[4,5] the ECF of the ChG suspended waveguide is ~9 times larger than those of other rectangular waveguides.[38] The LoD of the 1-cm-long ChG rectangular waveguide sensor based on WMS is 396.7 ppm with an averaging time of 81.8 s,[5] which is 67 times larger than that of the ChG suspended waveguide sensor with the same technique and length. Due to a large ECF, the LoD of the suspended waveguide sensor based on DAS is still 13 times lower than that of the ChG trapezoid waveguide sensor with the same length based on WMS.[5] Our sensor (WG_1) is also used for CO_2 sensing at 4319 nm, which shows the ability of wideband multigas detection. The above results show that combining a ChG nanorib suspended waveguide and the WMS technique improves the performance of a wideband on-chip gas sensor. At present, the waveguide loss needs to be further reduced. This can be realized by optimizing the thermal evaporation and lithography processes to reduce the surface roughness of the waveguide. Minimizing the waveguide loss and increasing the sensing waveguide length can increase the 2*f* signal and therefore improve the performance of the sensor.

In addition to WMS, other methods can also increase the sensitivity of the on-chip gas sensor according to different application requirements. Coating the waveguide surface with a material (such as a hyperbranched carbosilane polymer, polyhexamethylene biguanide, etc.) that absorbs specific gases can enhance the absorption, but the response time is longer.[39,40] Fabricating a metal island film on the waveguide with surface-enhanced infrared absorption effect can enhance gas absorption, but the increased absorption loss and scattering loss from the metal island film increase the waveguide loss.[4]

Table 2. MIR Wideband Sensing Characteristics of the ChG Suspended Nanorib Waveguide Sensors

Waveguide	ECF (%)	LoD (ppm)	Saturation optical power (mW)	N_{eff}	Reflectivity
WG_1	112 (@3291 nm)	103	67	1.08	0.001479
WG_1	110 (@4319 nm)	140	4	1.03	0.000218
WG_2	110 (@7625 nm)	194	44	1.02	0.000098

CONCLUSIONS

In summary, an ultra-wideband MIR ChG suspended nanorib waveguide gas sensor structure with exceptionally high ECF beyond free-space was proposed. Three waveguide sensors with different dimensional parameters were fabricated by a two-step lift-off method without dry etching. The operating waveband of the three suspended waveguides covers 3.2–5.6 μm, 5.4–8.2 μm, and 8.1–11.5 μm, respectively. Each waveguide has an >3 times larger waveband than the nonsuspended waveguide. The ECFs of the three waveguides are in the range of 107–116%, 107–116%, and 116–128%, respectively. A CH_4 sensing experiment at 3291 nm was used to illustrate the advantages of the suspended waveguide. The LoD of WMS measurement is 5.9 ppm with an optimum averaging time of 64.2 s, which is ~5 times smaller than that of DAS. The CO_2 sensing performances at 4319 nm and CH_4 at 7625 nm based on WMS were also experimentally studied. The experimentally derived ECFs are 112%, 110%, and 110%, respectively, at 3291 nm (WG_1), 4319 nm (WG_1), and 7625 nm (WG_2). The saturation optical power and reflectivity were studied. The ultra-wideband MIR gas sensors with exceptionally high ECF bring possibilities for multigas sensing applications in coal-mine and atmosphere monitoring. In addition, the monolithic integration of laser array or optical frequency comb (OFC), detectors, and ChG suspended waveguides is helpful to the development of a MIR multianalyte detection platform in gas-phase or liquid-phase.

https://doi.org/10.1021/acsnano.3c02699
ACS Nano 2023, 17, 17761–17770

Table 3. Comparison between the ChG Suspended Nanorib Waveguide CH_4 Sensor and Other Reported MIR ChG Waveguide CH_4 Sensors

Ref	Waveguide type	Wavelength (μm)	Technique	L (cm)[a]	α_{int} (dB/cm)[b]	ECF (%)	LoD/τ (ppm/s)[c]
38	Rectangular	3.31	DAS	2	7	10	25000/—
21	Rectangular	3.31	DAS	0.5	8	12.5	10000/—
4	Rectangular	3.291	DAS	2	3.6	0.5	6100/50.6
This	Suspended	3.291	DAS	1	4.5	112	30.3/43.4
5	Trapezoid	3.291	WMS	1	1.5	7.8	396.7/81.8
5	Trapezoid	3.291	WMS	2	1.5	7.8	140.8/32.4
This	Suspended	3.291	WMS	1	4.5	112	5.9/64.2

[a]L: sensing waveguide length. [b]α_{int}: waveguide loss. [c]τ: averaging time.

METHODS

Fabrication Process. The two-step lift-off method fabrication process of the ChG suspended nanorib membrane waveguide is shown in Figure 2a. The planar layer with etching holes was fabricated by the first-step lift-off method. The oxide layer of the Si substrate was 2 μm. The maximum spin speed of the RN-218 negative photoresist (Suzhou Research Semiconductor) was 3000 rpm. The prebake temperature and time were 90 °C and 90 s, respectively. The exposure dose was set as 60 mJ/cm^2 and the developing time was 180 s. After the first lithography (ABM) and development by 2.38% NMD-W (tetramethylammonium hydroxide), two rows of photoresist columns with a thickness of ∼5.5 μm were formed. The postbake temperature and time were 110 °C and 90 s, respectively. In order to make the suspended structure more stable and convenient for the secondary lithography alignment, only two etching holes at both ends were retained in the right row in Figure 1a. The center distance between two neighboring holes in the left row in Figure 1a was 30 μm, and the center distance between the left and right rows was also 30 μm. Hard bake was not carried out because the oblique sidewall structure of the photoresist was easy to melt at high temperature, leading to failure of the lift-off method. A ChG layer was deposited by thermal evaporation (IT-302, LJUHV). The ChG planar layer with etching holes was formed by removing the photoresist columns with acetone. Then the ChG nanorib was fabricated by the second-step lift-off method with the same parameters as the first-step lift-off method. Finally, the suspended waveguide structure was formed by 40% HF wet etching for 120 s. The wet etching distance on one side of the etching hole is 45 μm, and the wet etching rate is ∼375 nm/s considering the etching time of 2 min. Note that, if the order of the two lift-off steps is reversed, w_1 may increase, resulting in the decrease of ECF. Magnetron sputtering can be used to fabricate a dense ChG film. However, the fabrication time is generally long and it is not easy to remove the photoresist by the lift-off method. Thermal evaporation has the advantages of short fabrication period and the photoresist being easy to remove. So we used thermal evaporation to fabricate the ChG glass film.

Experimental Setup. The waveguide sensing system diagram is shown in Figure S4. A room-temperature distributed feedback (DFB) ICL (Nanoplus, Germany) was used as a laser source for CH_4 measurement. The temperature of the ICL was set as 16 °C by a temperature controller (TED200C, Thorlabs, USA). The output light from the ICL was TM polarized and a linear polarizer (LPMIR050, Thorlabs, USA) was used to control the waveguide mode. A current driver (LDC210C, Thorlabs, USA) was used to control the emitting wavelength of the ICL and cover the absorption line of CH_4 at 3291 nm. A reflective collimator (RC08, Thorlabs, USA) was used to couple the free-space light to a single-mode indium fluoride (InF_3) fiber (Le Verre Fluoré, France). The length of the suspended waveguide for gas sensing is 1 cm. A polydimethylsiloxane (PDMS) gas cell is bonded on the coupling region of the chip for the later sensing experiment. The InF_3 fiber is butt-coupled to the coupling waveguide with a measured coupling loss of ∼6 dB, and the output laser beam from the waveguide was probed by a detector (PVI-4TE-5, VIGO System, Poland). A data acquisition card (USB 6361, National Instruments) was used to acquire the sensing signal. The obtained signal was then processed with a LabVIEW platform for direct absorption spectroscopy (DAS) and wavelength modulation spectroscopy (WMS) measurement. Pure CH_4 (99.999%) was balanced by N_2 (99.999%) through a gas mixing system (Environics, Series 4000) to generate CH_4 samples with different concentration levels. These samples were used for the waveguide sensor measurement and characterization.

ASSOCIATED CONTENT

Supporting Information

The Supporting Information is available free of charge at https://pubs.acs.org/doi/10.1021/acsnano.3c02699.

Wideband characteristics of nonsuspended rectangular waveguide, optimization of chalcogenide suspended nanorib waveguide, cross interference characteristics of H_2O, wavelength modulation spectroscopy principle and sensing system, optimization of modulation depth, noise equivalent absorption sensitivity, saturation optical power of absorption, and etalon effects. (PDF)

AUTHOR INFORMATION

Corresponding Authors

Chuantao Zheng − *State Key Laboratory of Integrated Optoelectronics, College of Electronic Science and Engineering, Jilin University, Changchun 130012, China;* orcid.org/0000-0001-8008-466X; Email: zhengchuantao@jlu.edu.cn

Yu Zhang − *State Key Laboratory of Integrated Optoelectronics, College of Electronic Science and Engineering, Jilin University, Changchun 130012, China;* Email: yuzhang@jlu.edu.cn

Authors

Mingquan Pi − *State Key Laboratory of Integrated Optoelectronics, College of Electronic Science and Engineering, Jilin University, Changchun 130012, China*

Huan Zhao − *State Key Laboratory of Integrated Optoelectronics, College of Electronic Science and Engineering, Jilin University, Changchun 130012, China*

Zihang Peng − *State Key Laboratory of Integrated Optoelectronics, College of Electronic Science and Engineering, Jilin University, Changchun 130012, China*

Gangyun Guan − *State Key Laboratory of Integrated Optoelectronics, College of Electronic Science and Engineering, Jilin University, Changchun 130012, China*

Jialin Ji − *State Key Laboratory of Integrated Optoelectronics, College of Electronic Science and Engineering, Jilin University, Changchun 130012, China*

Yijun Huang − *State Key Laboratory of Integrated Optoelectronics, College of Electronic Science and Engineering, Jilin University, Changchun 130012, China*

https://doi.org/10.1021/acsnano.3c02699
ACS Nano 2023, 17, 17761−17770

Yuting Min − *State Key Laboratory of Integrated Optoelectronics, College of Electronic Science and Engineering, Jilin University, Changchun 130012, China*
Lei Liang − *State Key Laboratory of Luminescence and Applications, Changchun Institute of Optics Fine Mechanics and Physics, Chinese Academy of Sciences, Changchun 130033, China*
Fang Song − *State Key Laboratory of Integrated Optoelectronics, College of Electronic Science and Engineering, Jilin University, Changchun 130012, China*
Xue Bai − *State Key Laboratory of Integrated Optoelectronics, College of Electronic Science and Engineering, Jilin University, Changchun 130012, China;* orcid.org/0000-0003-2309-521X
Yiding Wang − *State Key Laboratory of Integrated Optoelectronics, College of Electronic Science and Engineering, Jilin University, Changchun 130012, China*
Frank K. Tittel − *Department of Electrical and Computer Engineering, Rice University, Houston, Texas 77005, United States*

Complete contact information is available at: https://pubs.acs.org/10.1021/acsnano.3c02699

Author Contributions

M.P. performed the experiment and optimization and wrote the manuscript. C.Z. and Y.W. supported the experiments. H.Z., Z.P., G.G., and J.J. conducted the experiment. Y.H. and Y.M. performed the simulation work. C.Z., L.L., F.S., X.B., Y.Z., Y.W., and F.K.T. provided technical guidance and helped to revise the paper.

Notes

The authors declare no competing financial interest.

ACKNOWLEDGMENTS

The authors wish to acknowledge the support in part by the National Natural Science Foundation of China (Nos. 62175087, 62235016, 61960206004, 62105118), in part by the Science and Technology Development Program of Jilin Province, China (Nos. 20200401059GX, 20230201054GX), in part by the Science and Technology Research Project of Department of Education, Jilin Province, China (No. JJKH20211088KJ), in part by the Key R&D Program of Changchun (No. 21ZGN24), and in part by the Program for JLU Science and Technology Innovative Research Team (JLUSTIRT, 2021TD-39).

REFERENCES

(1) Pi, M. Q.; Zheng, C. T.; Bi, R.; Zhao, H.; Liang, L.; Zhang, Y.; Wang, Y. D.; Tittel, F. K. Design of a Mid-Infrared Suspended Chalcogenide/Silica-on-Silicon Slot-Waveguide Spectroscopic Gas Sensor with Enhanced Light-Gas Interaction Effect. *Sens. Actuators B: Chem.* **2019**, *297*, 126732.
(2) Pi, M. Q.; Zheng, C. T.; Peng, Z. H.; Zhao, H.; Lang, J. M.; Liang, L.; Zhang, Y.; Wang, Y. D.; Tittel, F. K. Theoretical Study of Microcavity-Enhanced Absorption Spectroscopy for Mid-Infrared Methane Detection Using a Chalcogenide/Silica-on-Fluoride Horizontal Slot-Waveguide Racetrack Resonator. *Opt. Express* **2020**, *28* (15), 21432−21446.
(3) Pi, M. Q.; Zheng, C. T.; Zhao, H.; Peng, Z. H.; Lang, J. M.; Ji, J. L.; Liang, L.; Zhang, Y.; Wang, Y. D.; Tittel, F. K. Mid-infrared ChG-on-MgF2 Waveguide Gas Sensor Based on Wavelength Modulation Spectroscopy. *Opt. Lett.* **2021**, *46* (19), 4797−4800.
(4) Pi, M. Q.; Zheng, C. T.; Ji, J. L.; Zhao, H.; Peng, Z. H.; Lang, J. M.; Liang, L.; Zhang, Y.; Wang, Y. D.; Tittel, F. K. Surface-Enhanced Infrared Absorption Spectroscopic Chalcogenide Waveguide Sensor Using a Silver Island Film. *ACS Appl. Mater. Interfaces* **2021**, *13* (27), 32555−32563.
(5) Pi, M. Q.; Huang, Y. J.; Zhao, H.; Peng, Z. H.; Lang, J. M.; Ji, J. L.; Teng, L.; Song, F.; Liang, L.; Zhang, Y.; Zheng, C. T.; Wang, Y. D.; Tittel, F. K. Theoretical and Experimental Investigation of On-Chip Mid-Infrared Chalcogenide Waveguide CH_4 Sensor Based on Wavelength Modulation Spectroscopy. *Sens. Actuators B: Chem.* **2022**, *362*, 131782.
(6) Liu, W.; Ma, Y.; Liu, X.; Zhou, J.; Xu, C.; Dong, B.; Lee, C. Larger-Than-Unity External Optical Field Confinement Enabled by Metamaterial-Assisted Comb Waveguide for Ultrasensitive Long-Wave Infrared Gas Spectroscopy. *Nano Lett.* **2022**, *22* (15), 6112−6120.
(7) Zheng, K. Y.; Zheng, C. T.; Hu, L.; Song, F.; Zhang, Y.; Wang, Y. D.; Tittel, F. K. Near-Infrared Fiber-Coupled Off-Axis Cavity-Enhanced Thermoelastic Spectroscopic Sensor System for In Situ Multipoint Ammonia Leak Monitoring. *IEEE T. Instrum. Meas.* **2021**, *70*, 9510409.
(8) Zheng, K. Y.; Zheng, C. T.; Ma, N. N.; Liu, Z. D.; Yang, Y.; Zhang, Y.; Wang, Y. D.; Tittel, F. K. Near-Infrared Broadband Cavity-Enhanced Spectroscopic Multigas Sensor Using a 1650 nm Light Emitting Diode. *ACS Sens* **2019**, *4* (7), 1899−1908.
(9) Zheng, K. Y.; Yu, L.; Zheng, C. T.; Xi, Z. H.; Zhang, Y. X.; Yan, G.; Zhang, H. P.; Zhang, Y.; Wang, Y. D.; Tittel, F. K. Vehicle-Deployed Off-Axis Integrated Cavity Output Spectroscopic CH_4/C_2H_6 Sensor System for Mobile Inspection of Natural Gas Leakage. *ACS Sens* **2022**, *7* (6), 1685−1697.
(10) Liu, Z. W.; Zheng, C. T.; Zhang, T. Y.; Li, Y. F.; Ren, Q.; Chen, C.; Ye, W. L.; Zhang, Y.; Wang, Y. D.; Tittel, F. K. Midinfrared Sensor System Based on Tunable Laser Absorption Spectroscopy for Dissolved Carbon Dioxide Analysis in the South China Sea: System-Level Integration and Deployment. *Anal. Chem.* **2020**, *92* (12), 8178−8185.
(11) Yoo, K. M.; Midkiff, J.; Rostamian, A.; Chung, C. J.; Dalir, H.; Chen, R. T. InGaAs Membrane Waveguide: A Promising Platform for Monolithic Integrated Mid-Infrared Optical Gas Sensor. *ACS Sens* **2020**, *5* (3), 861−869.
(12) Ranacher, C.; Consani, C.; Tortschanoff, A.; Jannesari, R.; Bergmeister, M.; Grille, T.; Jakoby, B. Mid-infrared Absorption Gas Sensing Using A Silicon Strip Waveguide. *Sensor. Actuat. A: Phys.* **2018**, *277*, 117−123.
(13) Ranacher, C.; Consani, C.; Vollert, N.; Tortschanoff, A.; Bergmeister, M.; Grille, T.; Jakoby, B. Characterization of Evanescent Field Gas Sensor Structures Based on Silicon Photonics. *IEEE Photon. J.* **2018**, *10* (5), 2700614.
(14) Bi, R.; Pi, M. Q.; Zheng, C. T.; Zhao, H.; Liang, L.; Song, F.; Wang, D. D.; Zhang, Y.; Wang, Y. D.; Tittel, F. K. A Niobium Pentoxide Waveguide Sensor for On-Chip Mid-infrared Absorption Spectroscopic Methane Measurement. *Sens. Actuators B: Chem.* **2023**, *382*, 133567.
(15) Guan, G.; Liu, A. Q.; Zheng, C. T.; Pi, M. Q.; Zheng, K. Y.; Zhu, B. J.; Wu, X. Y.; Zheng, J.; Wang, Y. D.; Tittel, F. K. Numerical Investigation of on-Chip Multi-Gas Sensing Using a Low-Repetition-Frequency Microcavity Kerr Comb With Backward Interference Structure. *J. Lightwave Technol.* **2023**, *41* (10), 3208−3224.
(16) Kumari, B.; Barh, A.; Varshney, R. K.; Pal, B. P. Silicon-on-Nitride Slot Waveguide: A Promising Platform as Mid-IR Trace Gas Sensor. *Sens. Actuators B: Chem.* **2016**, *236*, 759−764.
(17) Kumari, B.; Varshney, R. K.; Pal, B. P. Design of Chip Scale Silicon Rib Slot Waveguide for Sub-Ppm Detection of N_2O Gas at Mid-IR Band. *Sens. Actuators B: Chem.* **2018**, *255*, 3409−3416.
(18) Gutierrez-Arroyo, A.; Baudet, E.; Bodiou, L.; Lemaitre, J.; Hardy, I.; Faijan, F.; Bureau, B.; Nazabal, V.; Charrier, J. Optical Characterization at 7.7 μm of An Integrated Platform Based on Chalcogenide Waveguides for Sensing Applications in the Mid-Infrared. *Opt. Express* **2016**, *24* (20), 23109−23117.
(19) Gutierrez-Arroyo, A.; Baudet, E.; Bodiou, L.; Nazabal, V.; Rinnert, E.; Michel, K.; Bureau, B.; Colas, F.; Charrier, J. Theoretical

Study of An Evanescent Optical Integrated Sensor for Multipurpose Detection of Gases and Liquids in the Mid-Infrared. *Sens. Actuators B: Chem.* **2017**, *242*, 842−848.
(20) Lin, H. T.; Kim, C. S.; Li, L.; Kim, M.; Bewley, W. W.; Merritt, C. D.; Canedy, C. L.; Vurgaftman, I.; Agarwal, A.; Richardson, K.; Hu, J.; Meyer, J. R. Monolithic Chalcogenide Glass Waveguide Integrated Interband Cascaded Laser. *Opt. Mater. Express* **2021**, *11* (9), 2869−2876.
(21) Su, P.; Han, Z.; Kita, D.; Becla, P.; Lin, H.; Deckoff-Jones, S.; Richardson, K.; Kimerling, L. C.; Hu, J.; Agarwal, A. Monolithic On-Chip Mid-IR Methane Gas Sensor with Waveguide-Integrated Detector. *Appl. Phys. Lett.* **2019**, *114* (5), 051103.
(22) Wang, Y. F.; Chen, W. W.; Wang, P. J.; Dai, S. X.; Li, J.; Li, Y.; Fu, Q.; Dai, T. G.; Yu, H.; Yang, J. Y. Ultra-High-Power-Confinement-Factor Integrated Mid-Infrared Gas Sensor Based on the Suspended Slot Chalcogenide Glass Waveguide. *Sens. Actuators B: Chem.* **2021**, *347*, 130466.
(23) Singh, R.; Su, P.; Kimerling, L.; Agarwal, A.; Anthony, B. W. Towards On-Chip Mid Infrared Photonic Aerosol Spectroscopy. *Appl. Phys. Lett.* **2018**, *113* (23), 231107.
(24) Huang, Y. W.; Kalyoncu, S. K.; Zhao, Q. C.; Torun, R.; Boyraz, O. Silicon-on-Sapphire Waveguides Design for Mid-IR Evanescent Field Absorption Gas Sensors. *Opt. Commun.* **2014**, *313*, 186−194.
(25) Kita, D. M.; Michon, J.; Johnson, S. G.; Hu, J. J. Are Slot and Sub-Wavelength Grating Waveguides Better than Strip Waveguides for Sensing? *Optica* **2018**, *5* (9), 1046−1054.
(26) Vlk, M.; Datta, A.; Alberti, S.; Yallew, H. D.; Mittal, V.; Murugan, G. S.; Jagerska, J. Extraordinary Evanescent Field Confinement Waveguide Sensor for Mid-infrared Trace Gas Spectroscopy. *Light: Sci. Appl.* **2021**, *10* (1), 26.
(27) Vlk, M.; Datta, A.; Alberti, S.; Murugan, G. S.; Aksnes, A.; Jagerska, J. Free-Standing Tantalum Pentoxide Waveguides for Gas Sensing in the Mid-Infrared. *Opt. Mater. Express* **2021**, *11* (9), 3111−3124.
(28) Ottonello-Briano, F.; Errando-Herranz, C.; Rodjegard, H.; Martin, H.; Sohlstrom, H.; Gylfason, K. B. Carbon Dioxide Absorption Spectroscopy with a Mid-Infrared Silicon Photonic Waveguide. *Opt. Lett.* **2020**, *45* (1), 109−112.
(29) Zhu, Y.; Wan, L.; Chen, Z. S.; Yang, Z. L.; Xia, D.; Zeng, P. Y.; Song, J. C.; Pan, J. S.; Feng, Y. M.; Zhang, M. J.; Liu, W. P.; Li, J. P.; Zhang, B.; Li, Z. H. Effects of Shallow Suspension in Low-Loss Waveguide-Integrated Chalcogenide Microdisk Resonators. *IEEE J. Lightwave Technol.* **2020**, *38* (17), 4817−4823.
(30) Kita, D.; Lin, H. T.; Li, J. Y.; Han, Z. H.; Su, P.; Gu, T.; Agarwal, A.; Yadav, A.; Richardson, K.; Hu, J. J. Suspended Chalcogenide Microcavities for Ultra-Sensitive Chemical Detection. In *2016 IEEE Sensors Conference*, Orlando, FL, USA, October 30−November 3, 2016; IEEE; 2016, pp 1−3.
(31) Chen, Z. S.; Wan, L.; Song, J. C.; Pan, J. S.; Zhu, Y.; Yang, Z. L.; Liu, W. P.; Li, J. P.; Gao, S. C.; Lin, Y. S.; Zhang, B.; Li, Z. H. Optical, Mechanical and Thermal Characterizations of Suspended Chalcogenide Glass Microdisk Membrane. *Opt. Express* **2019**, *27* (11), 15918−15925.
(32) Robinson, J. T.; Preston, K.; Painter, O.; Lipson, M. First-Principle Derivation of Gain in High-Index-Contrast Waveguides. *Opt. Express* **2008**, *16* (21), 16659−16669.
(33) Hu, J. J.; Tarasov, V.; Carlie, N.; Feng, N. N.; Petit, L.; Agarwal, A.; Richardson, K.; Kimerling, L. Si-CMOS-Compatible Lift-Off Fabrication of Low-Loss Planar Chalcogenide Waveguides. *Opt. Express* **2007**, *15* (19), 11798−11807.
(34) Li, C. G.; Zheng, C. T.; Dong, L.; Ye, W.; Tittel, F. K.; Wang, Y. D. Ppb-Level Mid-Infrared Ethane Detection Based on Three Measurement Schemes Using a 3.34-μm Continuous-Wave Interband Cascade Laser. *Appl. Phys. B: Laser Opt.* **2016**, *122* (7), 185.
(35) Zheng, K. Y.; Zheng, C. T.; Zhang, H. P.; Li, J. H.; Liu, Z. D.; Chang, Z. Y.; Zhang, Y.; Wang, Y. D.; Tittel, F. K. Near-Infrared Off-Axis Integrated Cavity Output Spectroscopic Gas Sensor for Real-Time, In Situ Atmospheric Methane Monitoring. *IEEE Sens. J.* **2021**, *21* (5), 6830−6838.
(36) *HITRAN Database*. https://hitran.org/ (accessed June 18, 2023).
(37) Castrillo, A.; DeTommasi, E.; Gianfrani, L.; Sirigu, L.; Faist, J. Doppler-Free Saturated-Absorption Spectroscopy of CO2 at 4.3 μm by Means of A Distributed Feedback Quantum Cascade Laser. *Opt. Lett.* **2006**, *31* (20), 3040−3042.
(38) Han, Z.; Lin, P.; Singh, V.; Kimerling, L.; Hu, J.; Richardson, K.; Agarwal, A.; Tan, D. T. H. On-Chip Mid-Infrared Gas Detection Using Chalcogenide Glass Waveguide. *Appl. Phys. Lett.* **2016**, *108* (14), 141106.
(39) Stievater, T. H.; Pruessner, M. W.; Park, D.; McGill, R. A.; Kozak, D. A.; Furstenberg, R.; Holmstrom, S. A.; Khurgin, J. B. Trace Gas Absorption Spectroscopy Using Functionalized Microring Resonators. *Opt. Lett.* **2014**, *39* (4), 969−972.
(40) Lang, J. M.; Pi, M. Q.; Zhao, H.; Peng, Z. H.; Ji, J. L.; Huang, Y. J.; Zheng, C. T.; Wang, X. B.; Zhang, D. M.; Wang, Y. D. Double-Slot Subwavelength Grating Waveguide for On-Chip Carbon Dioxide Sensing. *Microw. Opt. Techn. Lett.* **2023**, *65* (5), 1146−1151.

https://doi.org/10.1021/acsnano.3c02699
ACS Nano 2023, 17, 17761−17770